

Control of the VIV of a cantilevered square cylinder with free-end suction

Li Ying, Li Shiqing, Zeng Lingwei and Wang Hanfeng*

School of civil engineering, Central South University, Changsha, China

(Received September 7, 2018, Revised February 26, 2019, Accepted February 28, 2019)

Abstract. A steady slot suction near the free-end leading edge of a finite-length square cylinder was used to control its aerodynamic forces and vortex-induced vibration (VIV). The freestream oncoming flow velocity (U_∞) was from 3.8 m/s to 12.8 m/s. The width of the tested cylinder $d = 40$ mm and aspect ratio $H/d = 5$, where H was the height of the cylinder. The corresponding Reynolds number was from 10,400 to 35,000. The tested suction ratio Q , defined as the ratio of suction velocity (U_s) at the slot over the oncoming flow velocity at which the strongest VIV occurs (U_v), ranged from 0 to 3. It was found that the free-end slot suction can effectively attenuate the VIV of a cantilevered square cylinder. In the experiments, the RMS value of the VIV amplitude reduced quickly with Q increasing from 0 to 1, then kept approximately constant for $Q \geq 1$. The maximum reduction of the VIV occurs at $Q = 1$, with the vibration amplitude reduced by 92% , relative to the uncontrolled case. Moreover, the overall fluctuation lift of the finite-length square cylinder was also suppressed with the maximum reduction of 87%, which occurred at $Q = 1$. It was interesting to discover that the free-end shear flow was sensitive to the slot suction near the leading edge. The turbulent kinetic energy (TKE) of the flow over the free end was the highest at $Q = 1$, which may result in the strongest mixing between the high momentum free-end shear flow and the near wake.

Keywords: vortex-induced vibration; cantilevered square cylinder; steady suction; flow control

1. Introduction

Vortex-induced vibration (VIV) is a classic fluid-structure interaction phenomenon, which has long been the subject of fundamental and engineering investigations, especially the VIV of a two-dimensional (2D) cylinder. Our understanding of the VIV of a 2D cylinder has been significantly deepened in the last two decades, which has been reviewed in Chen *et al.* (1995), Khalak and Williamson (1997a), Cheng *et al.* (2003), Jauvtis and Williamson (2003), Sarpkaya (2004), Williamson and Govardhan (2004), Gabbai and Benaroya (2005), Williamson and Govardhan (2008), Bearman (2011), etc.

For a 2D circular cylinder, VIV occurs when the vortex shedding frequency matches with one of the natural frequencies of the cylinder. The amplitude of the VIV is closely related to the mass-damping ratio ($m^* \zeta$) (Khalak and Williamson 1997a, b) and Reynolds number (Re) (Raghavan and Bernitsas 2011), where m^* is the mass ratio and ζ is the damping ratio. Additionally, m^* is also an important parameter which determines both the branches of resonance (initial branch, upper branch, lower branch), the region of excitation, etc. (Feng 1968, Khalak and Williamson 1997b). The near wake behind an oscillating cylinder is also a long-established field of study. Up to now, four modes of vortex formation, including 2S mode, 2P mode, 2C mode and 2T mode, have been observed, e.g., Williamson and Roshko (1988), Williamson and Jauvtis (2004), Flemming and Williamson (2005), etc. Compared

with the VIV of a circular cylinder, there are fewer documents about the VIV of a square cylinder. Corless and Parkinson (1988) developed a quasi-steady model for simulating the VIV of a square cylinder. It was found that the model provided good quantitative predictions of the combined effects of both VIV and galloping, except for a modest over-prediction near the resonance region. For a square cylinder, the flow induced vibration is sensitive to its angle of attack α (Nemes *et al.* 2012, Zhao *et al.* 2014). When $\alpha = 0^\circ$ (face oriented to the oncoming flow), VIV is followed by significant transverse galloping with the increase of oncoming flow velocity. On the other hand, when $\alpha = 45^\circ$ (corner oriented to the oncoming flow), only VIV occurs, which is similar to that of a circular cylinder.

The diversified techniques used to control the aerodynamic forces and/or VIV of both 2D and three-dimensional (3D) bluff bodies can be classified into two categories, i.e., active and passive, depending on whether energy input is needed or not. The passive methods require no energy input and have been widely applied, such as external elements, roughness elements, helical grooves, strakes, etc. For example, cutting the corner of a square cylinder at the leading edge can significantly suppress the vortex shedding in its near wake (He *et al.* 2014). Besides, helical grooves and strakes were also found effective in suppressing the VIV of the circular cylinder (Huang 2011 and Zhou *et al.* 2011).

Similar to the passive methods, active control methods of different techniques have also been developed, such as moving-wall (Wu *et al.* 2007), dynamic controlled plate (Grager *et al.* 2011) and plasma actuators (Thomas *et al.* 2008). Recently, many documents have reported the effects

*Corresponding author, Professor
E-mail: wanghf@csu.edu.cn

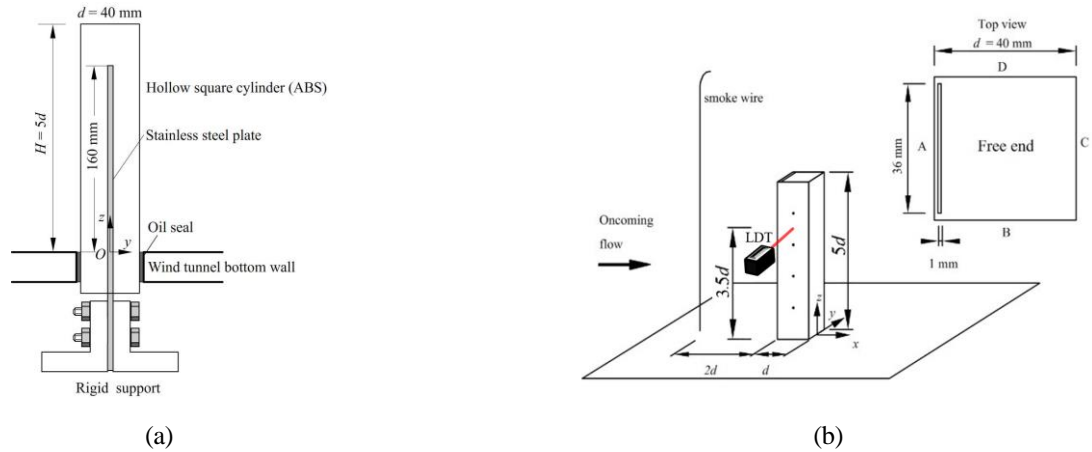


Fig. 1 Schematic of the experimental setup and the coordinate system

of suction/blowing on the aerodynamic forces and VIV of a 2D square cylinder. Çuhadaroğlu *et al.* (2007) discovered that the position and rate of injection had significant influences on the pressure coefficient and the drag coefficient of a square cylinder. Akansu and Firat (2010) experimentally investigated the manipulating functions with the slot jet from the rear face of a square prism. Sohankar *et al.* (2015) numerically investigated the effects of various combinations of suction and blowing around a square cylinder at low Reynolds numbers. They found the optimum configuration, with suction applied both side surfaces and blowing applied on the front and rear faces, had a maximum drag reduction of 72%.

However, a lot of structures in engineering applications are finite in length or height, such as high-rise buildings. Under the effects of the finite span, wall junction and free end, the flow around a wall-mounted finite-length structure is highly 3D and different drastically from that around a nominal 2D one (Rastan *et al.* 2017, Zhang *et al.* 2017, Sohankar *et al.* 2018). Relevant papers about the VIV and flow control for finite-length cylinders are far less than those for 2D bluff bodies.

Since the spanwise shear flow of a 3D square cylinder bears obvious similarities to that of the corresponding 2D square cylinder, the control methods for the latter are presumably still applicable to the former. Menicovich *et al.* (2014) successfully attenuated the aerodynamic forces of a finite-length rectangular cylinder, using steady tangential blowing along the spanwise leading edges. Steady slot suction at the spanwise leading edges was also found applicable for reducing the aerodynamic forces on a square cylinder with $H/d = 2.7$, where H and d are the height and width of the cylinder, respectively (Zheng and Zhang 2012). These suction/blowing control methods for 3D square bodies are essentially similar to those for 2D square cylinders. By weakening the spanwise flow separation, the fluctuating lift will be restrained.

Considering that the free-end shear flow of a 3D cylinder connects the spanwise shear flow from its both sides (Wang and Zhou 2009, Kawai *et al.* 2012, Rastan *et al.* 2017), the nature of the free-end shear flow may have remarkable effects on the entire near wake, especially for

the cylinders with relatively small H/d . In the previous study, it has been proved that the steady free-end slot suction can significantly suppress the overall aerodynamic forces of a finite-length square cylinder, especially its fluctuation lift (Wang *et al.* 2018). Nevertheless, it is still not clear whether the VIV of a cantilevered cylinder can be suppressed by manipulating its free-end shear flow. The present paper reports an experimental investigation on this topic. A steady slot suction near the free-end leading edge of a finite-length square cylinder was utilized to suppress its free-end shear flow and VIV. The effect of the suction ratio (Q) on the control results was also studied systematically.

2. Experimental details

2.1 Experimental setup

The experiments were conducted in an open-loop wind tunnel with a 1000 mm long square test section of 450 mm \times 450 mm. The maximum wind speed in this test section is 40 m/s, and the longitudinal turbulence intensity is less than 0.5%. The tested model contained two parts, i.e., an outer shell made of acrylonitrile butadiene styrene (ABS) using a 3D printer and a central stainless-steel plate. The length, width and thickness of the steel plate were 240 mm, 20 mm and 1.5 mm, respectively. As shown in Fig. 1(a), about 160 mm of the stainless-steel plate was inside the model. The surface of the model was polished and was smooth enough. The model penetrated through the wind tunnel bottom wall and mounted rigidly at a pedestal outside the test section, as shown in Fig. 1(a). The gap between the model and the wind tunnel bottom wall was less than 0.5 mm and was sealed with glycerol to prevent air leaking through it. The width d of the tested model was 40 mm and the effective $H/d = 5$, as shown in Fig. 1(a). The mass ratio of the tested model was 250. After the installation, the model was pushed slightly from its equilibrium position and released to vibrate freely. The lateral displacement of the model was measured by a laser displacement transducer. The natural frequency (f_0) and damping ratio (ζ) of the model could then be determined, which were 11.37 Hz and 0.7 %, respectively.

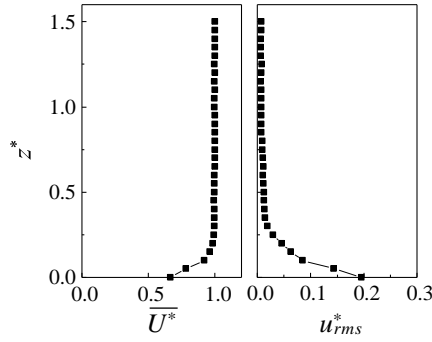


Fig. 2 Distribution of $\overline{U^*}$ and u_{rms}^* in the boundary layer on the bottom wall

As shown in Fig. 1(b), the x , y and z axes were in the streamwise, lateral and spanwise directions, respectively. The blockage ratio caused by the model was about 3.9%, whose effect was neglected. During the experiments, the freestream oncoming flow velocity (U_∞) was from 3.8 m/s to 12.8 m/s. The corresponding Reynolds number ($= U_\infty d/\nu$, where ν is the kinematic viscosity of air) was from 10,400 to 35,000. Relative to the structure with a curved surface, e.g. a circular cylinder, the aerodynamic characteristics of a finite-length square cylinder with $H/d = 5$ are less sensitive to Reynolds number (Wang *et al.* 2017). Thus, the main findings and conclusions of the present investigation may be also applicable at higher Reynolds numbers.

The suction slot was located at the cylinder free end, 1 mm ($0.025d$) downstream from its leading edge, as shown in Fig. 1(b). The total length of the slot was 36 mm ($0.9d$), and the width was 1 mm ($0.025d$). A steady suction was established at the slot using a vacuum pump located outside of the test section. The flow rate of the vacuum pump was monitored with a volume flow meter. Consequently, the mean suction velocity (U_s) at the slot could be calculated based on the mean volume flow rate and the area of the slot. The power of the vacuum pump could be adjusted continuously to control U_s . The suction ratio Q , defined as U_s/U_v (U_v is the oncoming flow velocity at which the maximum VIV occurs), was varied from 0 to 3, to test its effects on the control results.

The boundary layer on the wind tunnel bottom wall was documented using a Cobra probe (TFI, Series 100) at the position of the cylinder axis prior to its installation. The sampling frequency of the Cobra probe was 2 kHz, and the sampling duration for each measurement point was 20 s. $\overline{U^*}$ represents the time-averaged streamwise velocity and u_{rms}^* is the root-mean-square (RMS) value of the streamwise fluctuation velocity, respectively. The superscript “*” in the present paper indicates normalization with U_∞ and/or d . Fig. 2 presents the distributions of $\overline{U^*}$ and u_{rms}^* on the bottom wall. The overbar “ $\overline{\quad}$ ” denotes time-average in the present paper. The boundary layer thickness was about $0.25d$. That is, most of the cylinder span was in uniform oncoming flow with the turbulence intensity of approximately 0.5%.

2.2 Measurement techniques

Pressure on two side faces of the tested square cylinder was measured at four spanwise locations, i.e., $z^* = 1, 2, 3$ and 4, simultaneously. At each spanwise location, two pressure taps were installed at the center of the side faces B and D, respectively, as shown in Fig. 1(b). The sampling frequency of the pressure transducer was 2,000 Hz. A total of 20,000 instantaneous samples were collected for each channel. The reason why only eight pressure taps were used in the present experiment is that the effective damping ratio of the tested model will be increased if more pressure taps and tubes were installed, which may suppress the VIV amplitude and thus jeopardizing the observation. Each tap was connected to a pressure transducer using a PVC tube with a length of about 25 cm and the inner diameter of 0.6 mm. According to the phase-averaged pressure distribution around a square cylinder, the pressure on the cylinder side faces is quite uniform during the whole vortex shedding circle (Noda and Nakayama 2003). Thus, the pressure measured by each of the pressure taps (as shown in Fig. 1(b)) can be considered as the averaged pressure on the side face at certain z^* . Consequently, it is acceptable to estimate the instantaneous sectional lift coefficient based on the pressure measured at only the center points of side faces B and D via Eq. (1)

$$C_{l_z} = (P_{Bz} \cdot d - P_{Dz} \cdot d) / 0.5 \cdot \rho \cdot U_\infty^2 \cdot d = C_{PBz} - C_{PDz} \quad (1)$$

where C_{l_z} is the instantaneous lift coefficient at the spanwise location of z^* , P_{Bz} and P_{Dz} are the instantaneous pressure measured at the same z^* . C_{PBz} and C_{PDz} are the corresponding instantaneous pressure coefficient. The sectional fluctuation lift coefficient C'_{l_z} is the RMS value of the 20,000 instantaneous C_{l_z} . Besides, the overall instantaneous lift on the whole tested cylinder can be estimated by the weighted average values of the four sectional results along the cylinder span using the Eq. (2)

$$C_l = (1.5C_{l1} + C_{l2} + C_{l3} + 1.5C_{l4}) / 5 \quad (2)$$

where C_l is the overall instantaneous lift coefficient on the model, and C_{l1} , C_{l2} , C_{l3} and C_{l4} are the instantaneous sectional lift coefficients at $z^* = 1, 2, 3$ and 4. Consequently, the overall fluctuation lift coefficient C'_l can then be calculated by the RMS value of the 20,000 instantaneous C_l .

In order to provide a benchmark for comparison and validate the present pressure measurement technique, measurement was also conducted for a rigid model with the same geometry as the aeroelastic model shown in Fig. 1. The rigid model measurement was conducted at $U_\infty = 4.8$ m/s, at which the maximum VIV occurs for the aeroelastic model.

A laser displacement transducer (LDT) was utilized to measure the vibration amplitude of the tested model. As shown in Fig. 1(b), the LDT was placed outside of the test section. The laser beam can go through the transparent wind tunnel side wall to conduct the measurement of the cross-wind vibration of the model in y direction. The height of the laser beam was $z^* = 3.5$. The vibration amplitude at the cylinder free end, i.e., $z^* = 5$, can then be calculated based on the measurement results of the LDT. Note that, the RMS

vibration amplitude A^* discussed in the following sections indicates that of the cylinder free end. In the experiments, the sampling frequency of the LDT was 2 kHz, and the sampling duration for each measurement was 20 s.

Both flow visualization and PIV measurement were conducted at the $y^* = 0$ plane over the cylinder free end to document the variation of free-end shear flow at different Q . Note that, for the flow visualization and PIV measurement, a rigid model with the same dimensions as that shown in Fig. 1 was used. Flow visualization was performed using the smoke-wire technique. The smoke-wire was placed about $2d$ upstream from the tested cylinder. Smoke was generated with silicon oil on the smoke-wire heated by a pulse current. The flow visualization was conducted at $U_\infty \approx 1.1$ m/s, corresponding to a Re of 3,000. The flow visualization images were then taken by a Canon 6D SLR camera synchronized with the pulse current. The PIV measurement was conducted at $U_\infty = 10$ m/s, corresponding to a Re of 27,000. The sampling frequency of the PIV system was 10 Hz, far smaller than the vortex shedding frequency. A total of 500 random snapshots were captured for each tested Q , to get the distribution of time-averaged velocity and turbulent kinetic energy over the free end.

2.3 Uncertainty analysis

The total uncertainties of experimental results are affected by the experimental environment and the uncertainties of measurement facilities, i.e., Cobra probe, pressure transducer and LDT. According to the error propagation formula (Çuhadaroglu *et al.* 2007), the uncertainty of $\overline{U^*}$, i.e., $u_{\overline{U^*}}$ (where $u(\)$ is the uncertainty of certain variable), can be evaluated from Eq. (3)

$$u_{\overline{U^*}} = \left[\left(\frac{\overline{U}}{\overline{U^*}} \frac{\partial \overline{U^*}}{\partial \overline{U}} u_{\overline{U}} \right)^2 + \left(\frac{U_\infty}{\overline{U^*}} \frac{\partial \overline{U^*}}{\partial U_\infty} u_{U_\infty} \right)^2 \right]^{0.5} \quad (3)$$

Using the partial derivatives, which were defined as

$$\frac{\partial \overline{U^*}}{\partial \overline{U}} = \frac{1}{U_\infty}; \quad \frac{\partial \overline{U^*}}{\partial U_\infty} = (-1) \frac{\overline{U}}{U_\infty^2} \quad (4)$$

The uncertainty of the $\overline{U^*}$ was obtained as

$$u_{\overline{U^*}} = [(u_{\overline{U}})^2 + ((-1) \cdot u_{U_\infty})^2]^{0.5} \quad (5)$$

The $u_{\overline{U}}$ and u_{U_∞} , which are affected by the finite number of data samples, the calibration device, air density, etc. Given a sample size greater than 50, the uncertainty from a finite number of data samples can be estimated by $1/\sqrt{N}$ (N is the number of data samples). For the present experiment, this part was estimated to be 0.5%. Other parts were evaluated to be about 2.5%. So the $u_{\overline{U}}$ and u_{U_∞} were about 3%. Thus, the total uncertainty of the $\overline{U^*}$ was evaluated to be 4.2%.

Following the procedure above, the $u_{u_{\text{rms}}^*}$ and u_{A^*} were estimated to be 4.6% and 3.2%, respectively.

Table 1 Uncertainty of parameters

Parameter	Uncertainty	Parameter	Uncertainty
A^*	3.2 %	\overline{U}	3 %
C_l	7.2 %	$\overline{U^*}$	4.2 %
C_l'	8 %	u_{rms}^*	4.6 %
C_{lz}	7.2 %	ρ	2.5 %
C_{lz}'	8 %	Δp	3 %
U_∞	3 %		

According to the error propagation formula and Eq. (1), the uncertainty of the instantaneous sectional lift coefficient was evaluated from Eq. (6)

$$u_{c_{lz}} = \left[\left(\frac{\Delta p}{C_{lz}} \frac{\partial C_{lz}}{\partial \Delta p} u_{\Delta p} \right)^2 + \left(\frac{\rho}{C_{lz}} \frac{\partial C_{lz}}{\partial \rho} u_\rho \right)^2 + \left(\frac{U_\infty}{C_{lz}} \frac{\partial C_{lz}}{\partial U_\infty} u_{U_\infty} \right)^2 \right]^{0.5} \quad (6)$$

Where $\Delta p = P_{Bz} - P_{Dz}$. Using the partial derivatives, which were defined as

$$\frac{\partial C_{lz}}{\partial \Delta p} = \frac{1}{\frac{1}{2}\rho U_\infty^2}; \quad \frac{\partial C_{lz}}{\partial \rho} = \frac{(-1)\Delta p}{\frac{1}{2}\rho^2 U_\infty^2}; \quad \frac{\partial C_{lz}}{\partial U_\infty} = \frac{(-2)\Delta p}{\frac{1}{2}\rho U_\infty^3} \quad (7)$$

The uncertainty of the instantaneous sectional lift coefficient was obtained as

$$u_{c_{lz}} = [(u_{\Delta p})^2 + ((-1) \cdot u_\rho)^2 + ((-2) \cdot u_{U_\infty})^2]^{0.5} \quad (8)$$

The $u_{\Delta p}$ depends on the precision limit of the pressure transducer, variation of ambient temperature, etc. was estimated to be 3%. The uncertainty of the air density, determined by ideal gas law, was considered to be 2.5%. Finally, the total uncertainty of the instantaneous sectional lift coefficient was evaluated to be

$$u_{c_{lz}} = [3^2 + ((-1) \cdot 2.5)^2 + ((-2) \cdot 3)^2]^{0.5} \times 100 \% = 7.2 \% \quad (9)$$

Similarly, the uncertainty of the C_{lz}' was estimated to be 8%.

According to the error propagation formula and Eq. (2), the uncertainty of the C_l was evaluated from Eq. (10)

$$u_{c_l} = \frac{\partial C_l}{\partial c_{l1}} u_{c_{l1}} + \frac{\partial C_l}{\partial c_{l2}} u_{c_{l2}} + \frac{\partial C_l}{\partial c_{l3}} u_{c_{l3}} + \frac{\partial C_l}{\partial c_{l4}} u_{c_{l4}} \quad (10)$$

Because $u_{c_{l1}}, u_{c_{l2}}, u_{c_{l3}}, u_{c_{l4}} = u_{c_{lz}} = 7.2 \%$, it can be obtained

$$u_{c_l} = \left[\frac{1.5}{5} + \frac{1}{5} + \frac{1}{5} + \frac{1.5}{5} \right] \times 7.2 \% = 7.2 \% \quad (11)$$

Accordingly, the uncertainty of C_l' was estimated to be 8%.

The uncertainties of different parameters discussed above are summarized in Table 1.

3. Results and discussions

3.1 Vibration amplitude

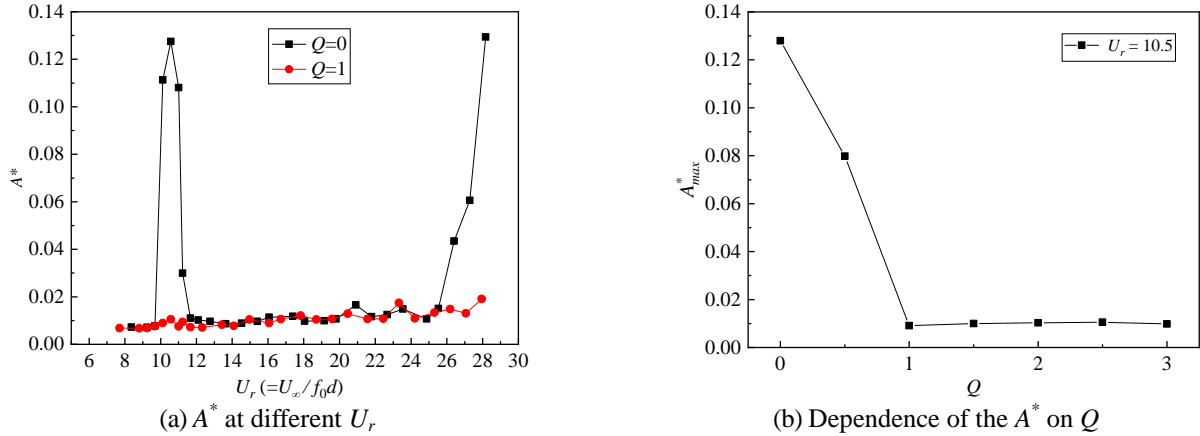


Fig. 3 The effects of Q on RMS value of the cross-wind displacement

To highlight the effects of the free-end suction on the VIV amplitude, Fig. 3(a) compares the normalized RMS values of lateral displacement (A^*) at different reduced velocity U_r ($=U_\infty/f_0d$) for $Q=0$ and 1. For the uncontrolled case, i.e., $Q=0$, it was found that with the increase of oncoming flow velocity, the lock-in occurs at U_r from 9.8 to 12. Note that, the maximum vibration occurs at $U_r = 10.5$, i.e., $U_\infty = 4.8$ m/s, which is used as the reference velocity for calculating the suction ratio Q . With the further increase of U_r , the vibration almost disappears for U_r ranging approximately from 12 to 25. However, for $U_r > 26$, A^* shoots up again abruptly, as shown in Fig. 3(a), which is related to the occurrence of galloping. For the case with $Q=1$, the lock-in region of the VIV almost disappears completely, as shown in Fig. 3(a). This observation suggests that the free end suction with $Q=1$ effectively suppresses the VIV of a cantilevered square cylinder. Moreover, the galloping which occurs at $U_r > 26$ is also postponed by the free-end suction, although it is not the primary concern of the present paper.

Fig. 3(b) shows the effect of Q on A^* of the cylinder measured with U_r of 10.5, at which the maximum vibration occurs. For the uncontrolled case ($Q=0$), $A^* = 0.12$. It reduces quickly with the increase of Q from 0 to 1. For the case with $Q=0.5$, $A^* = 0.08$, reducing by about 33% relative to the uncontrolled case. Interestingly, A^* reaches about 0.01 at $Q=1$. The maximum reduction in A^* is 92%, that is, the VIV in the lock-in region is almost completely suppressed at $Q=1$. The significant VIV disappears in all the cases with $Q > 1$, as shown in Fig. 3(b).

3.2 Fluctuating lift

Fig. 4 shows the variation of the overall fluctuating lift C_l' of the cylinder with the increase of Q . All the data shown in Fig. 4 were measured at the same U_r , as that used in Fig. 3(b). That is, the C_l' in Fig. 4 was the fluctuating lift measured in the lock-in region, where the maximum A^* occurs. For the uncontrolled case ($Q=0$), the present measured C_l' is 0.48. This maximum C_l' is far larger than the corresponding C_l' of 0.13 for a stationary finite-length

cylinder with the same H/d (Wang *et al.* 2018). This difference may be ascribed to the strong coupling effect in the lock-in region, which enhances the spanwise vortex shedding and thus results in a larger fluctuating lift. With the increase of Q , C_l' reduces quickly similar to the behavior of A^* , as shown in Fig. 3(b). At $Q=1$, the C_l' is approximately 0.075 with the maximum reduction of 84%, which is similar to that reported by Wang *et al.* (2018) for a stationary finite-length square cylinder. It should be noticed that the control effects are much better than that observed by Akansu and Firat (2010) with the maximum reduction of 60% for the fluctuating pressure coefficient of a 2D square cylinder. So the control strategy for 3D square cylinders shows its priority than that for 2D models. This is excepted, since at $Q=1$, the cross-wind vibration almost disappears under the effect of the free-end suction. For $Q \geq 1$, the fluctuation lift coefficients keep approximately constant. Obviously, the minimum C_l' also presents at $Q=1$, corresponding to the maximal reduction of amplitude, relative to the uncontrolled case ($Q=0$).

It is also interesting to know the effects of free-end suction on the sectional fluctuating lift C_{lz}' at different spanwise positions since the flow around a wall-mounted finite-length cylinder is highly 3D.

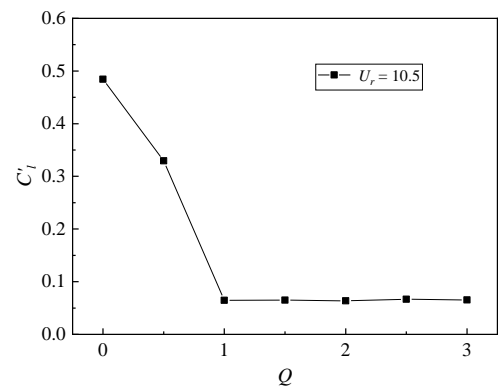


Fig. 4 Dependence of the overall fluctuating lift coefficient C_l' on Q

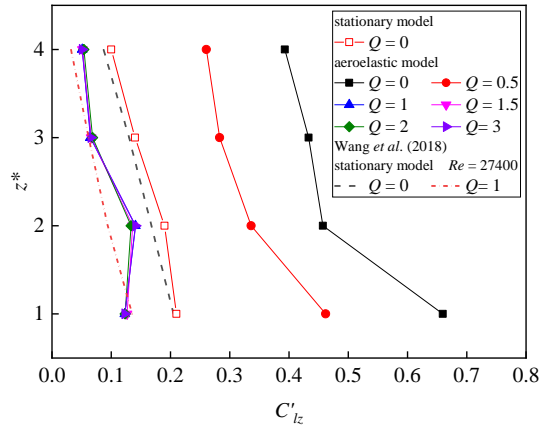


Fig. 5 Sectional fluctuating lift coefficients along the cylinder span ($U_r = 10.5$)

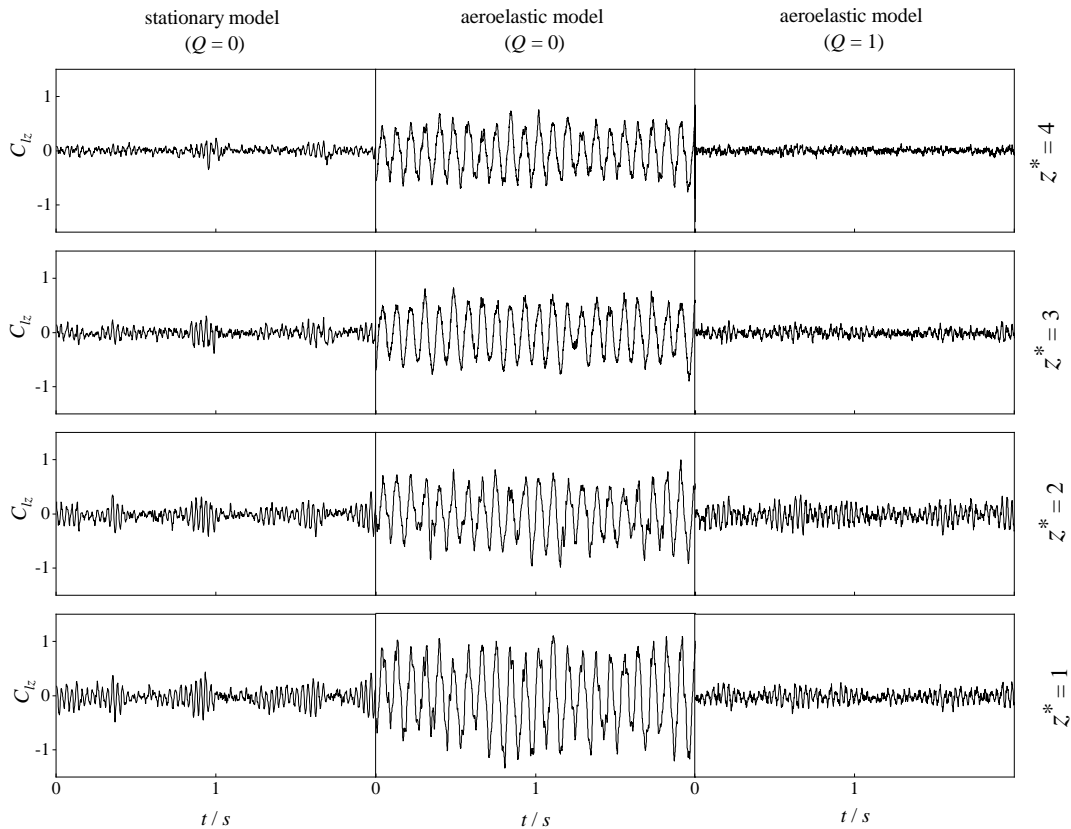


Fig. 6 The typical instantaneous signals of sectional lift coefficient for various Q and z^* ($U_\infty = 4.8$ m/s)

Fig. 5 presents the C'_{Lz} along the cylinder span at different Q , ranging from 0 to 3. Note that the result of the rigid stationary model is also included for comparison. For the rigid model, the present measured C'_{Lz} is quite similar to that reported by Wang *et al.* (2018). Although most of the cylinder span is immersed in uniform oncoming flow (see Fig. 2), it is obvious that C'_{Lz} is not constant along the cylinder span. C'_{Lz} is the smallest at $z^* = 4$ and increases gradually with the bottom wall approached. Moreover, the C'_{Lz} at $z^* = 2.5$ (the mean value of C'_{Lz} at $z^* = 2$ and 3) is 0.16, which is far smaller than the corresponding value of a

2D square cylinder of about 1.05-1.18 as reported by Tamura and Miyagi (1998) and Noda and Nakayama (2003). This is because the downwash flow tends to attenuate spanwise vortex shedding (Wang *et al.* 2006), thus resulting in a smaller fluctuating lift.

For the uncontrolled aeroelastic model, i.e., $Q = 0$, the C'_{Lz} is much larger than the stationary case. This observation suggests that the strong coupling in lock-in region enhances the spanwise vortex shedding noticeably for the present tested model.

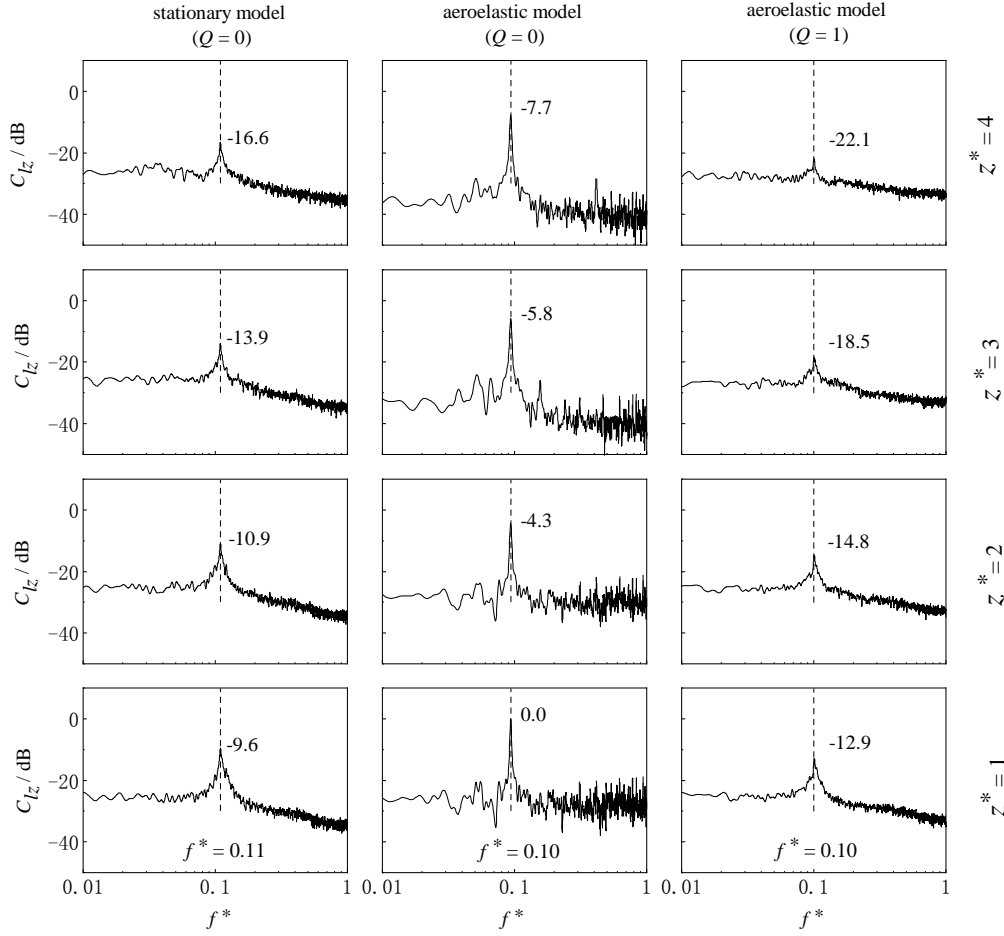


Fig. 7 Power spectral density function of the sectional lift coefficient for various Q and z^* ($U_\infty = 4.8$ m/s)

For the controlled case with $Q \geq 1$, the C_{l_z}' at all measured spanwise positions is much smaller than the uncontrolled case. The maximum reduction of C_{l_z}' occurs at $Q = 1$, and the reduction rates of C_{l_z}' at all spanwise locations are all larger than 80%. Compared to the stationary model investigated by Wang *et al.* (2018), the sectional fluctuating lift can be attenuated by free-end suction with similar control results. It is interesting to note that, the free-end suction suppresses fluctuating lift not only near the free end, but also over the entire cylinder span. This observation suggests that the slot suction which manipulates the free-end shear flow can change the whole near wake flow and the aerodynamic forces over the entire cylinder span, then successfully suppress the VIV. It is worth mentioning that, for the present tested controlled cases with $Q \geq 1$, the distribution of C_{l_z}' along the cylinder span is independent of Q , and accords quite well with that reported by Wang *et al.* (2018) for a stationary model. This observation is not unexpected, since the vibration is almost ceased for $Q \geq 1$ (Fig. 4), thus the C_{l_z}' of the present tested model becomes similar to that of the stationary one.

To highlight the effects of free-end suction on the aerodynamic force, Fig. 6 presents the typical instantaneous signals of sectional lift coefficient and Fig. 7 shows the power spectral density function of the lift coefficient for

various Q and z^* . Again, the results of both stationary model and aeroelastic model were compared at $U_\infty = 4.8$ m/s, corresponding to the U_r of 10.5 for the later, at which the maximum VIV occurs. For the stationary model, the large amplitude fluctuation of C_{l_z} occurs intermittently due to the two typical vortex shedding modes occur randomly in the near wake of a finite-length square cylinder (Wang and Zhou 2009, Sattari *et al.* 2012, Uffinger *et al.* 2013). While for the aeroelastic model, with $Q = 0$, C_{l_z} presents strong periodic fluctuation with large amplitude. Noted that the frequency of these signals is the same as the natural frequency of the square cylinder because of the intense resonance. When the free-end slot suction is applied with $Q = 1$, the fluctuation of C_{l_z} attenuates drastically. Moreover, the variation of fluctuation amplitude of C_{l_z} also retreats relative to the stationary model case, which may suggest the shifting between the two typical vortex shedding modes disappears.

In Fig. 7, all the spectra are normalized to dB scale using the highest peak value of C_{l_z}' , which occurs at $z^* = 1$ of the aeroelastic model with $Q = 0$. There are obvious peaks presence at $f^* = 0.11$ for the stationary model and $f^* = 0.10$ for the aeroelastic model. These predominant frequencies are lower than the corresponding value of a 2D square cylinder of about 0.13 (Wang *et al.* 2017). The

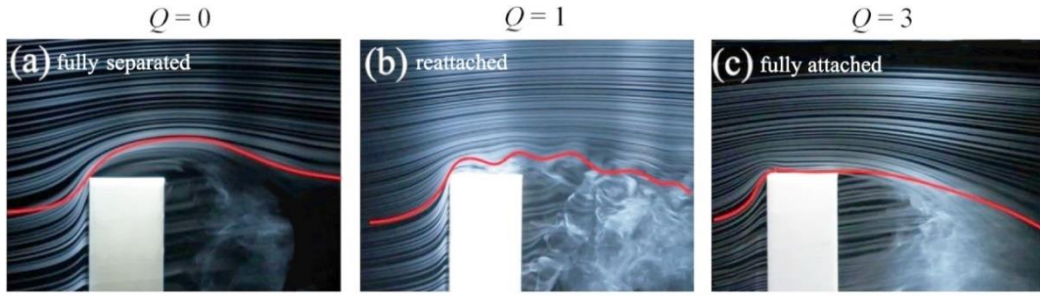


Fig. 8 Flow visualization of the free-end shear flow at different Q ($U_\infty = 1.1$ m/s)

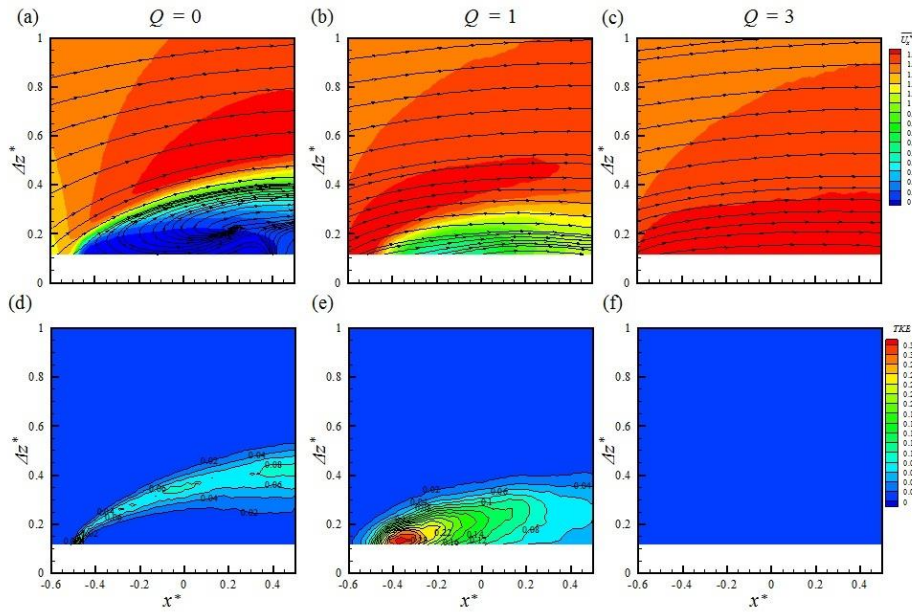


Fig. 9 Distribution of mean velocity and TKE over the free end: (a-c) $\overline{U_x^*}$ and mean streamlines; (d-f) TKE. ($U_\infty = 10$ m/s)

reason is that the free-end downwash flow separates the spanwise shear flow and prolongs the spanwise vortex shedding (Zdravkovich 2003). Besides, the peak values decrease gradually with the increase of z^* , suggesting that the periodicity of spanwise vortex shedding is weakened under the free-end effects. As expected, the spectral peak of C_{Lz} for the aeroelastic model with $Q = 0$ is much stronger than that of the stationary model, which inherently consists with that revealed in Fig. 5. For the aeroelastic model with $Q = 1$, the spectral peak becomes suppressed, relative to that of the uncontrolled case. Moreover, the peak values at all z^* are smaller than the those of stationary model case.

3.3 Free-end shear flow

Fig. 8 shows the flow visualization results in the symmetric plane at $y^* = 0$ over the cylinder free end. The solid red line in Fig. 8 indicates the shape of the free-end shear layer. Note that, the suction ratios were calculated based on U_∞ of 1.1 m/s, which was used for the flow visualization experiments.

For the uncontrolled case, the shear flow separates from the free-end leading edge and overshoots the cylinder. This shear flow bends towards the ground and forms a downwash at about $2d$ downstream from the cylinder. This downwash flow interacts with the spanwise shear flow in the near wake, resulting in the special aerodynamic characteristics of a finite-length cylinder (Tamura and Miyagi 1999). For the controlled case with $Q = 1$, the free-end shear flow separates at the leading edge and reattaches on it at approximately $0.5d$ downstream (Fig. 8(b)), forming a recirculation bubble on the free end. It is observed that the free-end shear flow becomes quite unstable under the effect of leading-edge suction, which is characterized by a wavy motion as moving downstream (Fig. 8(b)). This wavy free-end shear flow may enhance the interaction between the free-end shear flow and spanwise vortex shedding, thus suppress the fluctuating lift effectively. With the further increase of Q to 3, the separation bubble on the free end disappears completely. The shear flow becomes fully attached on the free end, as shown in Fig. 8(c).

Fig. 9 shows the distribution of time-averaged streamwise velocity $\overline{U_x^*}$ together with streamlines and turbulent kinetic energy (TKE) over the cylinder free end measured by PIV. Since the PIV used in the present experiment is a 2D system, the definition of TKE is thus given by $u'^2 + w'^2 / 2U_\infty^2$, where u' , w' the variances of the fluctuation velocities in x and z directions, respectively.

As shown in Figs. 8(a)-8(c), the shape of free-end shear flow agrees well with the flow visualization results shown in Fig. 8. At $Q = 0$, the oncoming flow separates at the free-end leading edge forming a flow reversal zone, as indicated by the streamlines shown in Fig. 9(a). Correspondingly, the high TKE region is limited within the shear layer over the free end (Fig. 9(d)). At $Q = 1$, the separation of the shear flow is significantly suppressed relative to that at $Q = 0$. However, the recirculation bubble revealed by the flow visualization (Fig. 8(b)) is not observed. This is because the PIV measurement region locates $0.1d$ higher than the free end to avoid surface reflection, thus it cannot capture the recirculation bubble on the free end, as shown in Fig. 8(b). It is interesting to note that, at $Q = 1$, the TKE is much higher than that at the uncontrolled case. Moreover, the region dominated by high TKE is also far larger than that of the uncontrolled case. High TKE corresponds to strong momentum transportation. That is, the interaction between the free-end shear flow and spanwise vortices may be enhanced by leading-edge suction with $Q = 1$. With the further increase of Q to 3, the separation on the free end is suppressed completely. Since the oncoming flow fully attaches on the free end without separation, the high TKE region over the free end also disappears, as shown in Fig. 9(f).

4. Conclusions

The present paper proposes a novel aerodynamic control method with steady suction at the free end of a cantilevered square cylinder to suppress its VIV. A steady slot suction near the leading edge of the free end was utilized to manipulate the free-end shear flow. The tested suction ratio Q , defined as the ratio of the suction velocity at which the slot to the oncoming flow velocity at the maximum VIV occurred, ranged from 0 to 3. Based on the experimental investigation, the following conclusions can be drawn:

- Steady free-end slot suction can significantly suppress the overall fluctuation lift of the finite-length square cylinder. Relative to the uncontrolled case, the overall fluctuating lift decreased with Q increasing from 0 to 1. The maximum reduction of C_l' was 87%, which occurred at $Q = 1$. At $Q \geq 1$, the reduction rate of the fluctuating lift (C_{l_z}') was always higher than 80% at all spanwise positions. It suggests that the steady slot suction suppresses the aerodynamic forces not only near the cylinder free end but also over the entire cylinder span.
- Steady free-end slot suction can significantly suppress the VIV of the finite-length square cylinder. The maximum RMS value of the lateral displacement of the

model reduced rapidly with the increase of Q from 0 to 1, then kept approximately constant with $Q \geq 1$. The maximum reduction of the maximum RMS value occurred at $Q = 1$, which reached 92%.

- The free-end shear flow is sensitive to the slot suction near the leading edge. At $Q = 0$, the oncoming flow separated at the leading edge and overshoot the free end. At $Q = 1$, the oncoming flow reattached on the free end forming a recirculation bubble. The TKE of the flow over the free end was the highest at $Q = 1$, which may result in the strongest mixing of the high momentum shear flow and the near wake.

Acknowledgments

The authors wish to acknowledge the support given to them from NSFC through Grants 11472312.

References

- Akansu, Y.E. and Firat, E. (2010), "Control of flow around a square prism by slot jet injection from the rear surface", *Exp. Therm. Fluid Sci.*, **34**(7), 906-914. <https://doi.org/10.1016/j.expthermflusci.2010.02.007>.
- Bearman, P.W. (2011), "Circular cylinder wakes and vortex-induced vibrations", *J. Fluid. Struct.*, **27**(5-6), 648-658. <https://doi.org/10.1016/j.jfluidstructs.2011.03.021>
- Chen, S.S., Zhu, S. and Cai, Y. (1995), "An unsteady flow theory for vortex-induced vibration", *J. Sound Vib.*, **184**(1), 73-92. <https://doi.org/10.1006/jsvi.1995.0305>.
- Cheng, L., Zhou, Y. and Zhang, M.M. (2003), "Perturbed interaction between vortex shedding and induced vibration", *J. Fluid. Struct.*, **17**(7), 887-901. [https://doi.org/10.1016/S0889-9746\(03\)00042-2](https://doi.org/10.1016/S0889-9746(03)00042-2).
- Corless, R.M. and Parkinson, G.V. (1988), "A model of the combined effects of vortex-induced oscillation and galloping", *J. Fluid. Struct.*, **2**(3), 203-220. [https://doi.org/10.1016/S0889-9746\(88\)80008-2](https://doi.org/10.1016/S0889-9746(88)80008-2).
- Çuhadaroğlu, B., Akansu, Y.E. and Turhal, A.Ö. (2007), "An experimental study on the effects of uniform injection through one perforated surface of a square cylinder on some aerodynamic parameters", *Exp. Therm. Fluid Sci.*, **31**(8), 909-915. <https://doi.org/10.1016/j.expthermflusci.2006.09.006>.
- Feng, C.C. (1968), "The measurement of vortex induced effects in flow past stationary and oscillating circular and D-section cylinders", Master's thesis, University of British Columbia, Vancouver, B. C., Canada.
- Flemming, F. and Williamson, C.H.K. (2005), "Vortex-induced vibrations of a pivoted cylinder", *J. Fluid Mech.*, **522**(522), 215-252. <https://doi.org/10.1017/S0022112004001831>.
- Gabbai, R.D. and Benaroya, H. (2005), "An overview of modeling and experiments of vortex-induced vibration of circular cylinders", *J. Sound Vib.*, **282**(3-5), 575-616. <https://doi.org/10.1016/j.jsv.2004.04.017>.
- Grager, T., Rothmayer, A. and Hu, H. (2011), "Stall Suppression of a Low-Reynolds-Number Airfoil with a Dynamic Burst Control Plate", *In 49th AIAA Aerospace Sciences Meeting Including the New Horizons Forum and Aerospace Exposition (p. 1180)*.
- He, G.S., Li, N. and Wang, J.J. (2014), "Drag reduction of square cylinders with cut-corners at the front edges", *Exp. Fluids*, **55**(6), 1745.

- Huang, S. (2011), "VIV suppression of a two-degree-of-freedom circular cylinder and drag reduction of a fixed circular cylinder by the use of helical grooves", *J. Fluid. Struct.*, **27**(7), 1124-1133. <https://doi.org/10.1016/j.jfluidstructs.2011.07.005>.
- Jauvtis, N. and Williamson, C.H.K. (2003), "Vortex-induced vibration of a cylinder with two degrees of freedom", *J. Fluid. Struct.*, **17**(7), 1035-1042. [https://doi.org/10.1016/S0889-9746\(03\)00051-3](https://doi.org/10.1016/S0889-9746(03)00051-3).
- Kawai, H., Okuda, Y. and Ohashi, M. (2012), "Near wake structure behind a 3d square prism with the aspect ratio of 2.7 in a shallow boundary layer flow", *J. Wind Eng. Ind. Aerod.*, **104-106**, 196-202. <https://doi.org/10.1016/j.jweia.2012.04.019>.
- Khalak, A. and Williamson, C.H.K. (1997a), "Investigation of relative effects of mass and damping in vortex-induced vibration of a circular cylinder", *J. Wind Eng. Ind. Aerod.*, **69-71**, 341-350. [https://doi.org/10.1016/S0167-6105\(97\)00167-0](https://doi.org/10.1016/S0167-6105(97)00167-0).
- Khalak, A. and Williamson, C.H.K. (1997b), "Fluid forces and dynamics of a hydroelastic structure with very low mass and damping", *J. Fluid. Struct.*, **11**(8), 973-982. <https://doi.org/10.1006/jfls.1997.0110>.
- Menicovich, D., Lander, D., Vollen, J., Amitay, M., Letchford, C. and Dyson, A. (2014), "Improving aerodynamic performance of tall buildings using fluid based aerodynamic modification", *J. Wind Eng. Ind. Aerod.*, **133**, 263-273. <https://doi.org/10.1016/j.jweia.2014.08.011>.
- Nemes, A., Zhao, J., Jacono, D. and Sheridan J. (2012), "The interaction between flow-induced vibration mechanisms of a square cylinder with varying angles of attack", *J. Fluid Mech.*, **710**, 102-130. <https://doi.org/10.1017/jfm.2012.353>.
- Noda, H. and Nakayama, A. (2003), "Free-stream turbulence effects on the instantaneous pressure and forces on cylinders of rectangular cross section", *Exp. Fluids*, **34**(3), 332-344.
- Raghavan, K. and Bernitsas, M.M. (2011), "Experimental investigation of Reynolds number effect on vortex induced vibration of rigid circular cylinder on elastic supports", *Ocean Eng.*, **38**(5-6), 719-731. <https://doi.org/10.1016/j.oceaneng.2010.09.003>.
- Rastan, M.R., Sohankar, A. and Alam, M.M. (2017), "Low-Reynolds-number flow around a wall-mounted square cylinder: Flow structures and onset of vortex shedding", *Phys. Fluids*, **29**(10), 103601. <https://doi.org/10.1063/1.4989745>.
- Sarpkaya, T. (2004), "A critical review of the intrinsic nature of vortex-induced vibrations", *J. Fluid. Struct.*, **19**(4), 389-447. <https://doi.org/10.1016/j.jfluidstructs.2004.02.005>.
- Sattari, P., Bourgeois, J.A. and Martinuzzi, R.J. (2012) "On the vortex dynamics in the wake of a finite surface-mounted square cylinder", *Exp. Fluids*, **52**(5), 1149-1167.
- Sohankar, A., Esfeh, M.K., Pourjafari, H., Alam, M.M. and Wang, L. (2018), "Features of the flow over a finite length square prism on a wall at various incidence angles", *Wind Struct.*, **26**(5), 317-329. <https://doi.org/10.12989/was.2018.26.5.317>.
- Sohankar, A., Khodadadi, M. and Rangraz, E. (2015), "Control of fluid flow and heat transfer around a square cylinder by uniform suction and blowing at low Reynolds numbers", *Comput. Fluids*, **109**, 155-167. <https://doi.org/10.1016/j.compfluid.2014.12.020>.
- Tamura, T. and Miyagi, T. (1999), "The effect of turbulence on aerodynamic forces on a square cylinder with various corner shapes", *J. Wind Eng. Ind. Aerod.*, **83**(1-3), 135-145. [https://doi.org/10.1016/S0167-6105\(99\)00067-7](https://doi.org/10.1016/S0167-6105(99)00067-7).
- Thomas, F.O., Kozlov, A. and Corke, T.C. (2008), "Plasma actuators for cylinder flow control and noise reduction", *AIAA J.*, **46**(8), 1921-1931. <https://doi.org/10.2514/1.27821>.
- Uffinger, T., Ali, I. and Becker, S. (2013) "Experimental and numerical investigations of the flow around three different wall-mounted cylinder geometries of finite length", *J. Wind Eng. Ind. Aerod.*, **119**, 13-27. <https://doi.org/10.1016/j.jweia.2013.05.006>.
- Wang, H.F. and Zhou, Y. (2009), "The finite-length square cylinder near wake", *J. Fluid Mech.*, **638**, 453-490. <https://doi.org/10.1017/S0022112009990693>.
- Wang, H.F., Peng, S., Li, Y. and He, X.H. (2018), "Control of the aerodynamic forces of a finite-length square cylinder with steady slot suction at its free end", *J. Wind Eng. Ind. Aerod.*, **179**, 438-448. <https://doi.org/10.1016/j.jweia.2018.06.016>.
- Wang, H.F., Zhao, X.Y., He, X.H. and Zhou, Y. (2017), "Effects of oncoming flow conditions on the aerodynamic forces on a cantilevered square cylinder", *J. Fluid. Struct.*, **75**, 140-157. <https://doi.org/10.1016/j.jfluidstructs.2017.09.004>.
- Wang, H.F., Zhou, Y., Chan, C.K. and Lam, K.S. (2006), "Effect of initial conditions on interaction between a boundary layer and a wall-mounted finite-length-cylinder wake", *Phys. Fluids*, **18**(6), 065106. <https://doi.org/10.1063/1.2212329>.
- Williamson, C. and Roshko, A. (1988), "Vortex formation in the wake of an oscillating cylinder", *J. Fluid. Struct.*, **2**(4), 355-381. [https://doi.org/10.1016/S0889-9746\(88\)90058-8](https://doi.org/10.1016/S0889-9746(88)90058-8).
- Williamson, C.H.K. and Jauvtis, N. (2004), "A high-amplitude 2T mode of vortex-induced vibration for a light body in XY motion", *Eur. J. Mech.-B/Fluids*, **23**(1), 107-114. <https://doi.org/10.1016/j.euromechflu.2003.09.008>.
- Williamson, C.H.K. and Govardhan, R. (2004), "Vortex-induced vibrations", *Annu. Rev. Fluid Mech.*, **36**, 413-455.
- Williamson, C.H.K. and Govardhan, R. (2008), "A brief review of recent results in vortex-induced vibrations", *J. Wind Eng. Ind. Aerod.*, **96**(6-7), 713-735. <https://doi.org/10.1016/j.jweia.2007.06.019>.
- Wu, C.J., Wang, L. and Wu, J.Z. (2007), "Suppression of the von kármán vortex street behind a circular cylinder by a travelling wave generated by a flexible surface", *J. Fluid Mech.*, **574**(574), 365-391. <https://doi.org/10.1017/S0022112006004150>.
- Zdravkovich, M.M. (2003), "Flow around circular cylinders", Applications, vol. 2.
- Zhang, D., Cheng, L., An, H. and Zhao, M. (2017), "Direct numerical simulation of flow around a surface-mounted finite square cylinder at low Reynolds numbers", *Phys. Fluids*, **29**(4), 045101. <https://doi.org/10.1063/1.4979479>.
- Zhao, J., Leontini, J.S., Jacono, D.L. and Sheridan, J. (2014), "Fluid-structure interaction of a square cylinder at different angles of attack", *J. Fluid Mech.*, **747**, 688-721. <https://doi.org/10.1017/jfm.2014.167>.
- Zheng, C.R. and Zhang, Y.C. (2012), "Computational Fluid Dynamics study on the performance and mechanism of suction control over a high-rise building", *Struct. Des. Tall Spec. Build.*, **21**(7), 475-491. <https://doi.org/10.1002/tal.622>.
- Zhou, T., Razali, S.M., Hao, Z. and Cheng, L. (2011), "On the study of vortex-induced vibration of a cylinder with helical strakes", *J. Fluid. Struct.*, **27**(7), 903-917. <https://doi.org/10.1016/j.jfluidstructs.2011.04.014>.